

## RESEARCH ARTICLE

10.1002/2015MS000436

## Key Points:

- Photosynthesis is nonlinear, computations on mean versus full fields will differ
- Sea ice drives spatial variability in light
- Accounting for nonlinearity improves accuracy of simulated primary productivity

## Correspondence to:

M. C. Long,  
mclong@ucar.edu

## Citation:

Long, M. C., K. Lindsay, and M. M. Holland (2015), Modeling photosynthesis in sea ice-covered waters, *J. Adv. Model. Earth Syst.*, 7, 1189–1206, doi:10.1002/2015MS000436.

Received 29 JAN 2015

Accepted 20 JUN 2015

Accepted article online 24 JUN 2015

Published online 31 JUL 2015

## Modeling photosynthesis in sea ice-covered waters

Matthew C. Long<sup>1</sup>, Keith Lindsay<sup>1</sup>, and Marika M. Holland<sup>1</sup>
<sup>1</sup>National Center for Atmospheric Research, Boulder, Colorado, USA

**Abstract** The lower trophic levels of marine ecosystems play a critical role in the Earth System mediating fluxes of carbon to the ocean interior. Many of the functional relationships describing biological rate processes, such as primary productivity, in marine ecosystem models are nonlinear functions of environmental state variables. As a result of nonlinearity, rate processes computed from mean fields at coarse resolution will differ from similar computations that incorporate small-scale heterogeneity. Here we examine how subgrid-scale variability in sea ice thickness impacts simulated net primary productivity (NPP) in a  $1^\circ \times 1^\circ$  configuration of the Community Earth System Model (CESM). CESM simulates a subgrid-scale ice thickness distribution and computes shortwave penetration independently for each ice thickness category. However, the default model formulation uses grid-cell mean irradiance to compute NPP. We demonstrate that accounting for subgrid-scale shortwave heterogeneity by computing light limitation terms under each ice category then averaging the result is a more accurate invocation of the photosynthesis equations. Moreover, this change delays seasonal bloom onset and increases interannual variability in NPP in the sea ice zone in the model. The new treatment reduces annual production by about 32% in the Arctic and 19% in the Antarctic. Our results highlight the importance of considering heterogeneity in physical fields when integrating nonlinear biogeochemical reactions.

## 1. Introduction

Net primary productivity (NPP) is a fundamental ecological and biogeochemical process. NPP supplies energy to higher trophic levels and places an upper limit on ecosystem production. In the ocean, NPP is a key determinant of the strength of the biological carbon pump and is thus an important component of the ocean carbon cycle. Accurate representation of NPP is an imperative for the marine biogeochemical components of Earth System models [Falkowski *et al.*, 2000].

Underlying the representation of NPP in models is a functional description of the relationship between the specific rate of photosynthetic carbon fixation ( $P$ ;  $\text{s}^{-1}$ ) and irradiance ( $I$ ;  $\text{W m}^{-2}$ ) under nutrient replete conditions. This is known as a PI-curve. The typical PI-curve for marine phytoplankton increases approximately linearly at low irradiance, then the rate of increase falls off before reaching a plateau at some irradiance beyond which photosynthesis is light saturated [Falkowski and Raven, 2007]. Photosynthetic rates decline at high irradiance levels due to photoinhibition, though this effect is often neglected in marine biogeochemical models [e.g., Moore *et al.*, 2002; Dutkiewicz *et al.*, 2005; Dunne *et al.*, 2010]. Notably, over the range of irradiance levels typical of the upper ocean, PI-curves are nonlinear and concave downward, such that

$$P\left(\frac{I_1 + I_2}{2}\right) \geq \frac{P(I_1) + P(I_2)}{2},$$

for any  $I_1$  and  $I_2$ .

Given the nonlinearity of the photosynthesis-irradiance relationship, integrating mean versus heterogeneous light fields leads to disparate results. This property of the PI-curve can impact model solutions in polar regions, where sea ice produces heterogeneous light distributions. In sea ice regions, surface ocean light environments can span a range from very little transmitted photosynthetically available radiation (PAR) under thick ice or heavy snow cover, to open water, which is exposed to the full downwelling irradiance.

Sea ice heterogeneity has been considered in modeling the climate of polar regions, where sea ice strongly mediates air-sea energy fluxes [McPhee, 2008]. Air-sea heat fluxes and ice growth have nonlinear functional

© 2015. The Authors.

This is an open access article under the terms of the Creative Commons Attribution-NonCommercial-NoDerivs License, which permits use and distribution in any medium, provided the original work is properly cited, the use is non-commercial and no modifications or adaptations are made.

dependence on ice thickness, which exhibits strong variability at spatial scales well below the typical resolution of climate models. This has motivated developing representations of subgrid-scale ice thickness distributions [Thorndike *et al.*, 1975]. Including a subgrid-scale ice thickness distribution improves a climate model's ability to represent ice formation and melt processes, which are critical to accurately simulating the seasonal cycle in sea ice cover and the transient response to greenhouse warming [Holland *et al.*, 2006]. In this paper, we explore an extension of the subgrid-scale treatment of ice thickness to investigate the impact of heterogeneous light fields on marine photosynthesis calculations.

Our objective is to evaluate the impact of subgrid-scale sea ice heterogeneity on aggregate photosynthetic rates computed in the Community Earth System Model (CESM) [Hurrell *et al.*, 2013], integrated at (nominal)  $1^\circ \times 1^\circ$  horizontal resolution. The sea ice component of CESM includes a subgrid-scale ice thickness distribution, but in the default model setup the ocean only receives grid-cell mean irradiance. We present a simple modification to the formulation for photosynthesis involving a change in the order of operations: instead of computing light limitation terms based on grid-cell mean irradiance, the new formulation averages the limitation terms computed under each subgrid-scale ice thickness category. This change accounts for subgrid-scale heterogeneity in light availability and yields a more accurate invocation of the model equations than the default approach. The impact of this new treatment is to significantly reduce simulated NPP in the sea ice zone, a manifestation of the downward concavity of the PI-curve.

The paper is organized as follows. Section 2 provides theoretical background on light transmittance through sea ice and the representation of light-limited photosynthesis. Section 3 describes the functional changes we have implemented in CESM, and the numerical experiments we performed to document their impact on model solutions. The results of these experiments are presented in section 4 and evaluated in section 5.

## 2. Theory

### 2.1. Optical Properties of Sea Ice

Sea ice and overlying snow intercept solar radiation, thereby diminishing irradiance supplied to the upper ocean. Radiative transfer in the sea ice component of CESM is based on a Delta-Eddington multiple scattering parameterization [Briegleb and Light, 2007]. The Delta-Eddington parameterization relies on inherent optical properties (IOPs) of sea ice, overlying snow, melt ponds, and other constituents, including black carbon and dust absorbers within the sea ice and overlying snow. As state variables (ice thickness, snow depth, surface ponding, temperature, etc.) change in time, IOPs are used to compute the evolution of surface albedos, internal absorption and transmission of shortwave through the sea ice system to the ocean. Snow has relatively efficient scattering properties, and thus, if present, significantly reduces light transmittance through the sea ice system [Briegleb and Light, 2007]. Meltwater ponds, by contrast, lower the surface albedo and scatter less, thereby increasing net light transmittance [Holland *et al.*, 2012]. For similar conditions (ice thickness, pond cover), the sea ice radiative transfer within CESM simulates a reasonable transmittance compared to Surface Heat Budget of the Arctic Ocean Project (SHEBA) field observations [Briegleb and Light, 2007]. However, while the Delta-Eddington scheme provides a fairly mechanistic representation of radiative transfer through the sea ice system, some processes are not represented in the model, and therefore only treated approximately. For instance, CESM does not prognostically represent algae in sea ice; thus, in the simulations we present, there is no enhanced shortwave absorption associated with algae within sea ice. This omission may cause the model to overestimate light transmittance in sea ice regions favorable to ice-algae growth.

### 2.2. Light-Limited Photosynthesis

In this analysis, we focus on the representation of light-limited photosynthesis in the Biogeochemical Element Cycle (BEC) model, which is the marine ecosystem component of CESM. In BEC, light limitation is computed as the ratio of the carbon-specific photosynthetic rate,  $P^C$  ( $\text{s}^{-1}$ ), to the maximum photosynthetic rate,  $P_{max}^C$  ( $\text{s}^{-1}$ ), and is computed as a function of irradiance,  $I$  ( $\text{W m}^{-2}$ ), using the Geider *et al.* [1998] dynamic growth model,

$$\mathcal{L}(I) = \frac{P^C}{P_{max}^C} = 1 - \exp(-I/I_k). \quad (1)$$

$P_{max}^C$  is computed as function of temperature and nutrient limitation [Moore *et al.*, 2002] and  $I_k$  ( $\text{W m}^{-2}$ ), which describes the light-saturation behavior of the PI-curve.

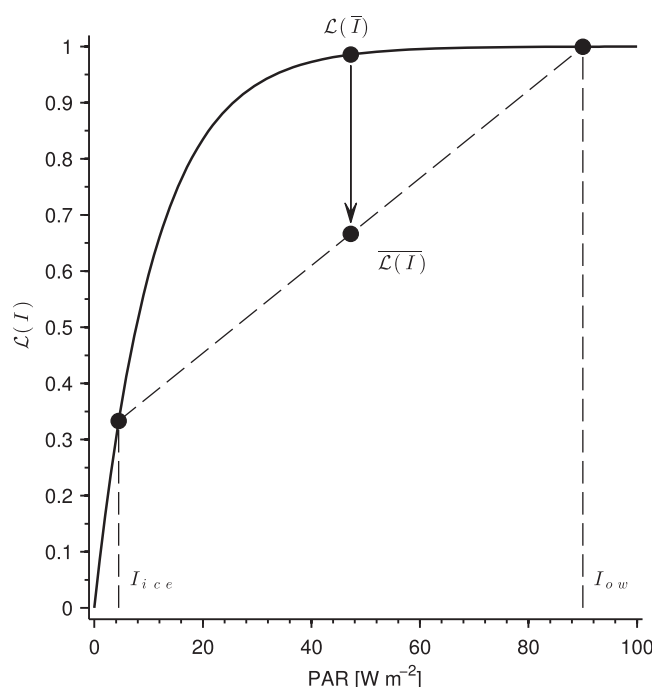


**Figure 1.** Relative rate of photosynthesis (equation (1)) plotted as a function of irradiance (photosynthetically available radiation [PAR]) under constant temperature (2°C), nutrient replete conditions, and a chlorophyll:carbon ratio of 0.025 g Chl (g C)<sup>-1</sup> ( $P_{max}^C = 4.8 \text{ day}^{-1}$ , representative of diatoms in BEC). A thought experiment is illustrated in which a grid-cell is half covered with sea ice that has uniform transmittance properties, passing 5% of incident solar radiation such that  $I_{ice} = 0.05 I_{ow}$ , where  $I_{ow}$  is the PAR value of open water.

In this expression,  $I_i$  is the open-water irradiance ( $i = 0$ ) or the irradiance at the ice-ocean interface under ice thickness categories  $i = 1 \dots n$ , and  $a_i$  is the fraction of grid-cell area accounted for by open water or ice thickness category ( $\sum_{i=0}^n a_i = 1$ ).

Changing the order of operations to compute  $\mathcal{L}$  for open water and each ice category, then averaging the result, yields

$$\overline{\mathcal{L}(I)} = \sum_{i=0}^n \mathcal{L}(I_i) a_i, \quad (2)$$

which is systematically lower than  $\mathcal{L}(\bar{I})$  due to the downward concavity of equation (1) (Figure 1).

The degree of discrepancy between  $\mathcal{L}(\bar{I})$  and  $\overline{\mathcal{L}(I)}$  will depend on the distribution of subgrid-scale irradiance and the contribution each category makes to the area-weighted mean. To illustrate this, we present an extension of the idealized experiment described above for a range of ice concentrations of uniform thickness (i.e.,  $n = 1$ ) and transmittance properties (Figure 2). In the limits where there is no ice or complete coverage,  $\overline{\mathcal{L}(I)}$  and  $\mathcal{L}(\bar{I})$  are identical. The discrepancy between  $\overline{\mathcal{L}(I)}$  and  $\mathcal{L}(\bar{I})$  increases with increasing ice coverage until an ice fraction of about 0.8, after which point the difference between the two functions begins to collapse back to zero (Figure 2c).

The gradients of the  $\mathcal{L}(\bar{I})$  and  $\overline{\mathcal{L}(I)}$  surfaces in ice-fraction-irradiance space are different, which has implications for variability in NPP. In particular, for incident irradiance values greater than about  $30 \text{ W m}^{-2}$  and ice fractions below about 0.8, the gradient in light limitation with respect to changes in ice fraction is greatly accentuated in the  $\overline{\mathcal{L}(I)}$  surface (Figure 2b) compared to the  $\mathcal{L}(\bar{I})$  surface (Figure 2a). Photosynthesis computations that sample sea ice variability in this region of enhanced gradient can thus be expected to yield greater variability in NPP using  $\overline{\mathcal{L}(I)}$  versus  $\mathcal{L}(\bar{I})$ . For instance, at a constant irradiance of  $50 \text{ W m}^{-2}$ , a change in ice fraction from 0.3 to 0.1 yields an increase in the light limitation function computed from grid-

$$I_k = \frac{P_{max}^C}{\alpha^{chl} \theta},$$

where  $\alpha^{chl}$  ( $\text{g C m}^{-2} (\text{g Chl W s})^{-1}$ ) is the initial slope of the chlorophyll *a* specific PI-curve and  $\theta$  is the chlorophyll to carbon ratio (g Chl:g C). The chlorophyll to carbon ratio,  $\theta$ , evolves prognostically in the model, thereby providing a representation of photoadaptation [Moore *et al.*, 2002].

Figure 1 shows  $\mathcal{L}(I)$  for a given set of physiological parameters ( $\theta$ ,  $\alpha^{chl}$ ) and nutrient replete, constant temperature conditions. An idealized thought experiment is shown: a grid-cell is 50% covered by ice with uniform transmittance properties (5% of incident light, which is a typical transmittance in CESM); the remaining portion of the cell is open water. In the standard computation, photosynthesis at the surface is computed using  $\mathcal{L}(\bar{I})$ , where  $\bar{I}$  is the area-weighted, grid-cell mean surface irradiance defined as

$$\bar{I} = \sum_{i=0}^n I_i a_i.$$

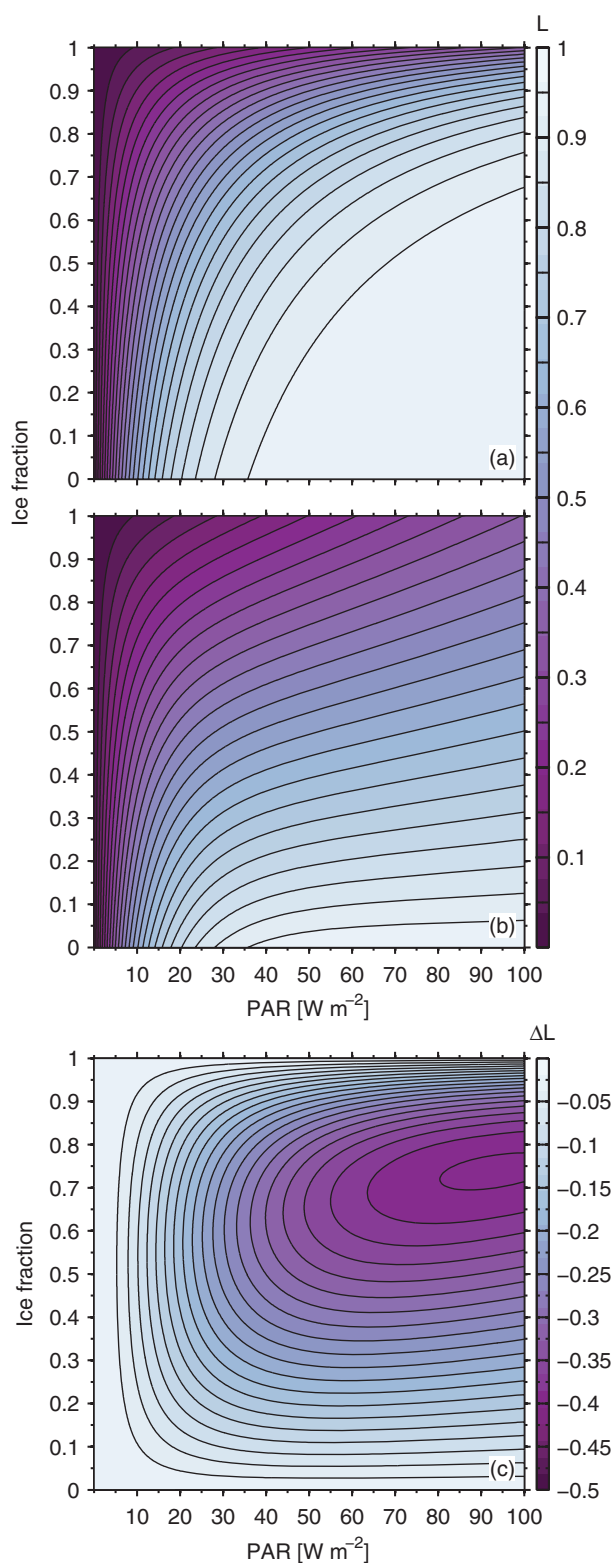


**Figure 2.** (a) Light limitation term computed as a function of grid-cell mean irradiance ( $\mathcal{L}(\bar{I})$ ) and (b) the mean of grid-cell limitation terms ( $\bar{\mathcal{L}}(\bar{I})$ ) plotted as a function of ice concentration and incident irradiance (assuming that ice transmits 5% of incident light). (c) Figure 2b minus Figure 2a.

cell mean irradiance ( $\mathcal{L}(\bar{I})$ ) of 0.02, from 0.96 to 0.98; using  $\bar{\mathcal{L}}(\bar{I})$ , by contrast yields lower values, but a much larger change from 0.75 to 0.91, a difference of 0.16.

### 3. Numerical Experiments

We ran experiments with CESM in fully coupled mode, meaning that the atmosphere, ocean, sea ice, and land surface component models were all integrated forward in time, exchanging information via the flux coupler [Gent et al., 2011]. The component setup we used is that of the recent CESM Large Ensemble (LE) project [Kay et al., 2014]. Briefly, the atmospheric model was the Community Atmospheric Model, version 5 (CAM5), integrated at nominal  $1^\circ \times 1^\circ$  horizontal resolution [Hurrell et al., 2013]. The ocean component is based on the Parallel Ocean Program, version 2 (POP2) [Smith et al., 2010]. POP2 was integrated with a nominal horizontal resolution of  $1^\circ \times 1^\circ$  and 60 vertical levels; the vertical grid spacing is 10 m in the upper 160 m and varies with depth below, increasing to 250 m by a depth of  $\sim 3500$  m, then remaining constant to the model bottom at 5500 m [Danabasoglu et al., 2012; Long et al., 2013]. The CESM sea ice component is the Los Alamos Sea Ice Model, version 4 (CICE4) [Hunke and Lipscomb, 2008] with some updates including prognostic melt ponds and the deposition and cycling of black carbon and dust aerosols [Holland et al., 2012]. CICE4 operates on the ocean horizontal grid, includes an elastic-viscous-plastic rheology, and represents a subgrid-scale ice thickness distribution with five ice thickness categories: (1) 0.1–0.64 m, (2) 0.64–1.4 m, (3) 1.4–2.5 m, (4) 2.4–4.6 m, and (5) 4.6–9.3 m. Ice thickness categories provide a means of discretizing the subgrid-scale distribution in sea ice thickness [Hunke and Lipscomb, 2008]. The BEC ecosystem model includes three phytoplankton functional types (diatoms, “small” pico/nanophytoplankton, and diazotrophs) and one adaptive zooplankton class [Moore et al., 2013]. Phytoplankton growth is determined as a

function of temperature, multnutrient (N, P, Si, and Fe) limitation, and light availability. Notably, while the default configuration of BEC simulates the basic structure of basin-wide chlorophyll distributions, *Moore et al.* [2013] find that simulated chlorophyll is too high over much of the Arctic, where the model predicts an intense summertime diatom bloom.

To change the order of operations in the photosynthesis calculation, the CESM flux coupler was modified to pass shortwave fluxes to the ocean from each ice category independently. We refer to this new configuration of the model as having a multicolumn ocean grid (MCOG), since in principle the column physics could be treated uniquely under each ice category [e.g., *Holland*, 2003]. In the experiments presented here, only light-related metabolic processes are impacted by the MCOG treatment. While we focus on photosynthesis in this paper, the MCOG treatment was also applied to the light threshold [*Moore et al.*, 2002] governing nitrification. We conducted two integrations with CESM: (1) “CTRL,” which has the default treatment of photosynthesis and (2) “MCOG,” in which photosynthesis is computed using equation (2). The MCOG photosynthesis computation relies on six unique values of surface irradiance (open water and five ice thickness categories) at each grid-cell; the vertical attenuation of light in the water column is performed for each category using the same grid-cell mean chlorophyll concentration.

Both experiments were preindustrial simulations in which external forcings were held constant at levels representative of year 1850. We ran preindustrial simulations, rather than twentieth century transient integrations to avoid computational costs associated with running the full historical period. Furthermore, the absence of externally forced trends simplifies the analysis documenting the effect of MCOG. The experiments were initialized using state information from the LE 1850-control integration at model-year 1001. The experiments were 30 years in duration, long enough to provide a reasonable sample of natural climate variability. The experiments differ only in their ecosystem dynamics: the physical climate, including the sea ice distribution, is bit-for-bit identical in the two simulations. Physical climate in the default CESM is affected by the marine ecosystem model via the dependence of the vertical profile of ocean shortwave absorption on chlorophyll. We turned this feedback off, however, to maximize comparability between CTRL and MCOG. Shortwave absorption in the physical model in our simulations then is computed from a climatological chlorophyll distribution (though light attenuation for the purposes of photosynthesis uses prognostic chlorophyll). This is not a critical detail in relation to our objectives, but it is worth noting that the new treatment of photosynthesis will change sea ice distributions by impacting chlorophyll and thus the shortwave absorption when this feedback is reenabled. Indeed, in preliminary experiments with the new photosynthesis treatment that included the prognostic chlorophyll shortwave-absorption dependence, sea ice cover increased modestly in spring and summer in response to reduced chlorophyll. This is consistent with the findings of *Lengaigne et al.* [2009], who show that chlorophyll blooms significantly impact simulated Arctic sea ice distributions in the IPSL-CM4 model.

## 4. Results

We present results from the numerical experiments in this section. As we state in section 1, the objective of this paper is to quantify the impact of nonlinearity on integrating the equations for photosynthesis in a heterogeneous light field, as simulated within CESM. In the context of this objective, the specific elements of the physical climate model that produce subgrid-scale heterogeneity in irradiance are not vital; we therefore focus the analysis on the impact of MCOG on NPP, rather than the mechanisms generating subgrid-scale variability in light transmittance through sea ice. As we discuss below, however, the importance of treating subgrid-scale variation in light increases with the subgrid-scale variance in irradiance. So models with higher subgrid-scale variation in light transmittance (i.e., more heterogeneous subgrid-scale ice thickness, snow or melt pond distributions) will be impacted more by the MCOG treatment; the converse is also true.

In some presentations, we aggregate results regionally. For the Arctic, we consider the region north of 65.5°N, which comprises an oceanic area of  $12.8 \times 10^6 \text{ km}^2$ . For the Antarctic, we consider the region south of 60°S, an oceanic area of  $19.4 \times 10^6 \text{ km}^2$ .

### 4.1. Sea Ice Simulation

Figure 3 shows the modeled 30 year climatology of sea ice area in each hemisphere, including modern (1981–2000) satellite-based observational estimates of ice area [*Comiso*, 2000]. The simulated Arctic ice pack



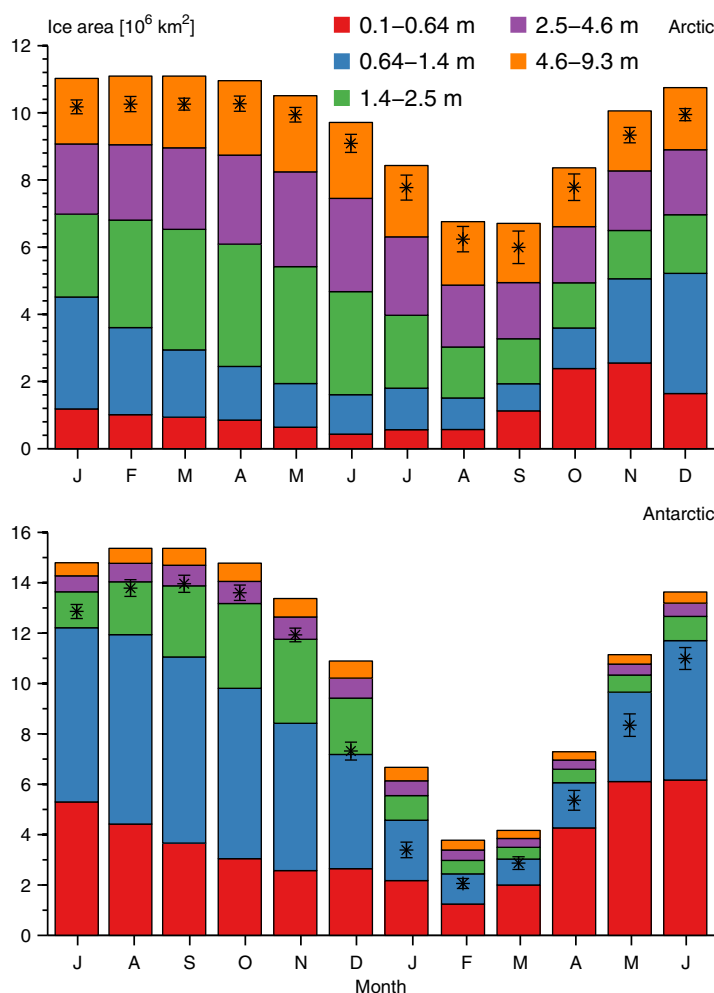


**Figure 3.** Monthly mean ice area by ice thickness category for the (top) Arctic ( $>65.5^{\circ}\text{N}$ ) and (bottom) Antarctic region ( $>60^{\circ}\text{S}$ ). Note the differing horizontal axes in this and subsequent figures; it has been shifted to align the hemispheres seasonally. The dots show the climatological monthly mean, total observed ice area from satellite,  $\pm 1\sigma$  over the period 1981–2000 [Comiso, 2000].

reaches minimal area in September; reductions in the intermediate ice thickness categories accomplish much of the seasonal reduction in coverage, whereas the volume of the thickest ice remains relatively constant throughout the year. *Jahn et al.* [2012] review the sea ice simulation in CCSM4, a version of the coupled model preceding the CESM configuration discussed here, and find that the overall distribution of thickness and ice extent is well captured by the model. The Arctic sea ice simulation in the CESM LE is not dramatically different from CCSM4, in spite of using a different atmosphere model (CAM5 versus CAM4). In the simulations presented here, the total ice area in the Arctic is somewhat larger than modern observational estimates [e.g., *Fetterer et al.*, 2002], though this is consistent with the preindustrial climate state of the integrations (Figure 3). The ice is also thicker than modern day estimates [e.g., *Kwok et al.*, 2009], with a higher fraction of the ice pack residing in thicker ice categories. The twentieth century simulations conducted with this same model version show very good agreement of northern hemisphere ice extent with satellite observations and a very reasonable ice thickness distribution [Holland and Landrum, 2015]; indeed, while the ice area is somewhat too large, the amplitude of seasonal variation is very similar to modern observations (Figure 3).

The Antarctic sea ice minimum is in February, with a much larger annual variation in sea ice area than the Arctic. A greater fraction of Antarctic sea ice is in the thinner ice categories, consistent with a generally younger pack and sea ice dynamics producing thinner ridges than in the Arctic. Previous versions of CESM (CCSM4) had Antarctic sea distributions that were much too extensive, with insufficient contraction of ice extent during the austral summer [Landrum et al., 2012]. The switch from CAM4 to CAM5 improved the

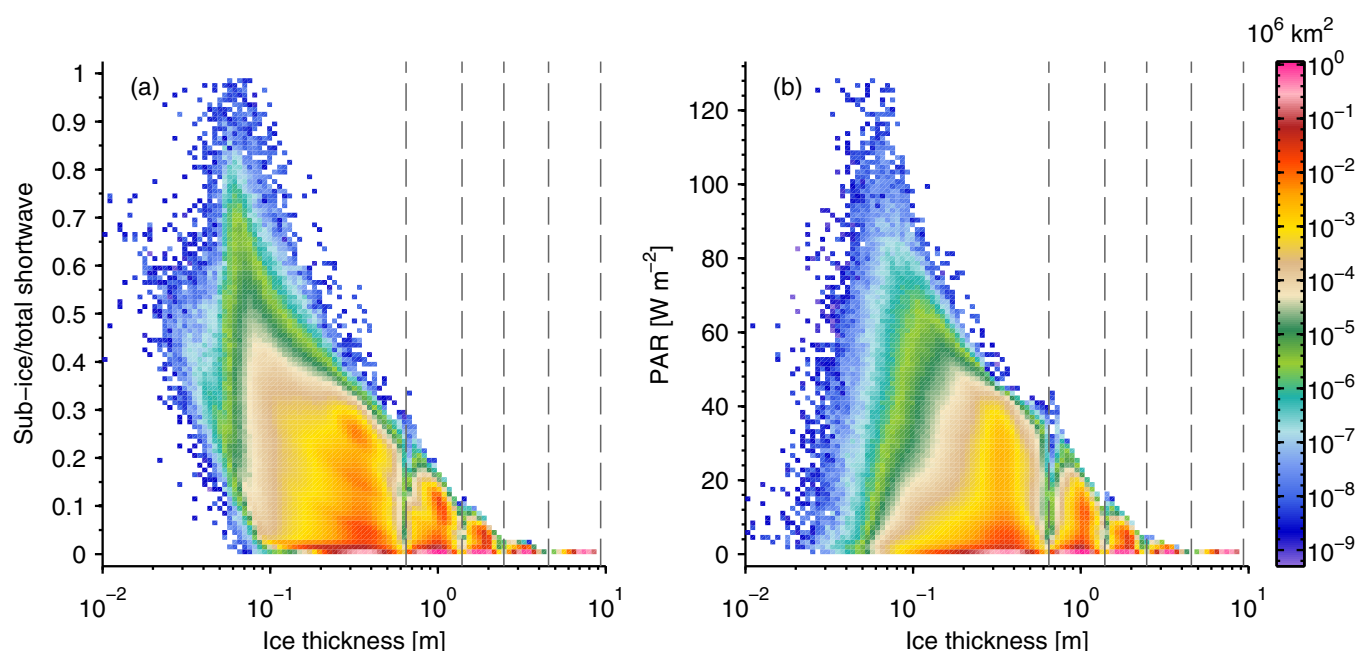


**Figure 4.** Joint distributions of (a) transmittance and (b) below-ice irradiance (photosynthetically available radiation) in CESM. Both have the same integral ( $16 \times 10^6 \text{ km}^2$ ), which is equal to the daily mean (over the 30 year integration), global-total, illuminated ice area. Vertical dashed lines show the boundaries of the ice thickness categories in CESM.

Antarctic simulation, likely a result of diminished Ekman transport of ice with more realistic winds [Meehl *et al.*, 2013]. As with the Arctic sea ice, the simulated Antarctic ice in the integrations presented here is generally thicker and more extensive (Figure 3) than observed estimates [e.g., Fetterer *et al.*, 2002; Worby *et al.*, 2008] and a larger fraction of the ice pack resides within the thicker ice categories. This is in part due to the preindustrial climate conditions; the simulated Antarctic ice area and thickness do generally decline over the twentieth century [Holland and Landrum, 2015].

#### 4.2. Light Environments

Variation in ice thickness (and related properties) produces a broad range of subice light environments in MCOG. Figure 4 shows the simulated global distribution of illuminated ice area as a function of the transmitted irradiance and ice thickness from the subgrid-scale sea ice calculations. The transmitted irradiance tends to diminish with increasing ice thickness; however, overlying snow and other factors mean that subice irradiance tends to be significantly less than what transmittance through pure ice would yield [Briegleb and Light, 2007]. Roughly 4.5% of the global illuminated ice area has subice irradiance values above about  $7.7 \text{ W m}^{-2}$ , sufficient to drive photosynthesis for the model's diatom functional type at about 50% of the light-saturated rate (e.g., Figure 1).

Figure 5 shows the seasonal evolution of regional-mean surface PAR for open water and under each ice thickness category in the Arctic and Antarctic. The open-water PAR in the Antarctic is slightly greater than in the Arctic due to the latitudinal boundaries defining these regions; greater cloudiness in the Arctic may also contribute to this difference, and also explains the greater short time scale variability in Arctic open-water PAR. Notably, subice PAR for the two thinnest ice categories tends to be greater in the Arctic, where less snow accumulates on the ice surface. In the Arctic, the mean PAR under the thinnest ice (0.1–0.64 m) is about 17% of the open water value during the summer season (Figure 5). The thickest ice in both regions transmits essentially no light.

#### 4.3. Seasonal Productivity

As expected from theoretical consideration (section 2.2), the revised treatment of photosynthesis reduces NPP in the sea ice zones of both hemispheres (Figure 6). Indeed, MCOG reduces annual production by about 32% in the Arctic and 19% in the Antarctic (Table 1). The reductions in NPP magnitude are

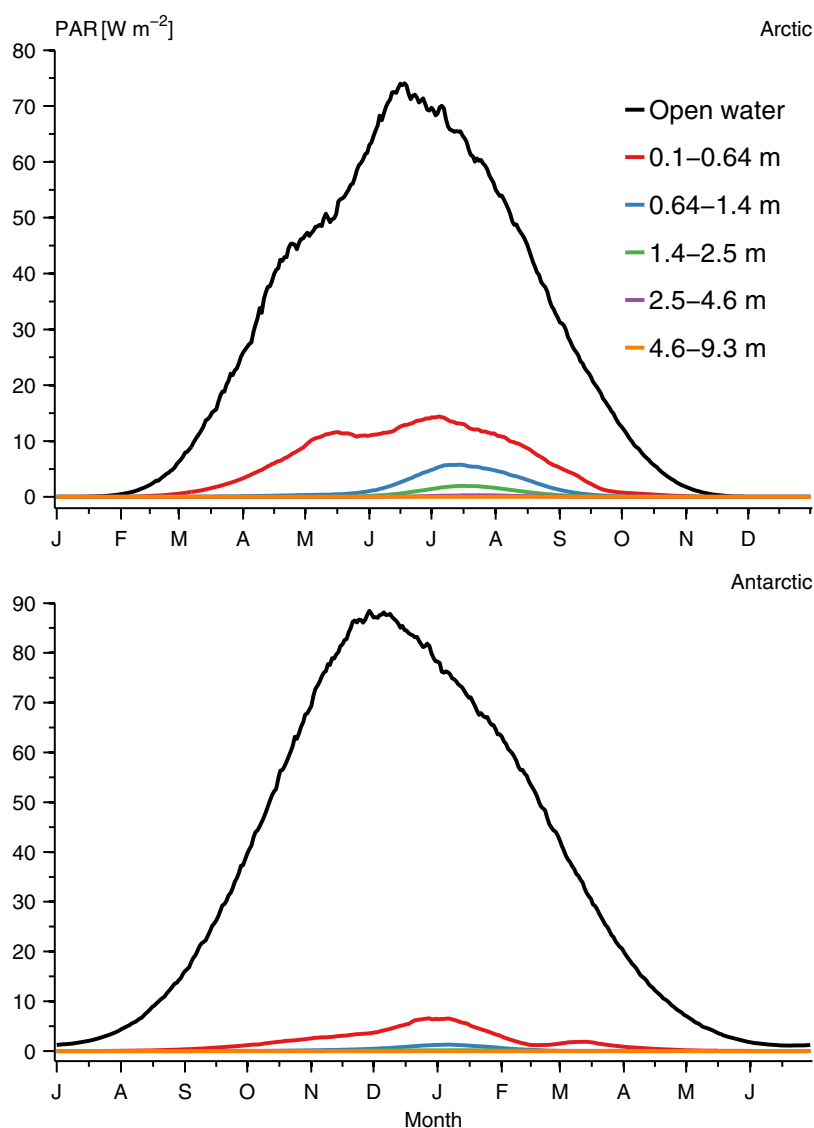


**Figure 5.** Regional-mean surface ocean photosynthetically available radiation (PAR) for the (top) Arctic ( $>65.5^{\circ}\text{N}$ ) and (bottom) Antarctic region ( $>60^{\circ}\text{S}$ ). Mean open-water and below-ice PAR for each ice thickness category is shown.

accompanied by changes in phenology. In the Arctic, the regional NPP cycle changes from a single bloom peaking in late-June to a double peaked bloom, the first in May followed by a second peak in July–August. The dominant phenological change in Antarctic NPP is a delay in the bloom peak; in CTRL, the Antarctic bloom peaks sharply in December and declines rapidly, whereas the MCOG bloom peaks in January.

The dual peaked Arctic bloom in MCOG (Figure 6) is explained by regional variation in NPP and a tighter coupling to the spatial patterns associated with sea ice retreat. The first peak in May corresponds to high NPP in relatively limited open water areas in the peripheral seas of the Arctic basin, primarily the high-latitude North Atlantic and Norwegian Sea (Figure 7). These regions of intense blooms encounter nutrient limitation and productivity declines in late-May into June, but while the pan-Arctic NPP continues to increase in CTRL following the annual cycle of PAR (Figure 6), pan-Arctic NPP declines in MCOG through early June corresponding to a delay imposed by ice cover over much of the basin. Arctic NPP increases in MCOG from mid-June through August; NPP in the central Arctic remains lower than CTRL, though August NPP in MCOG is slightly higher than CTRL on the periphery of the central basin (Figure 7). These local increases in NPP relative to CTRL are explained by alleviation of nutrient limitation associated with reduced consumption earlier in the season.



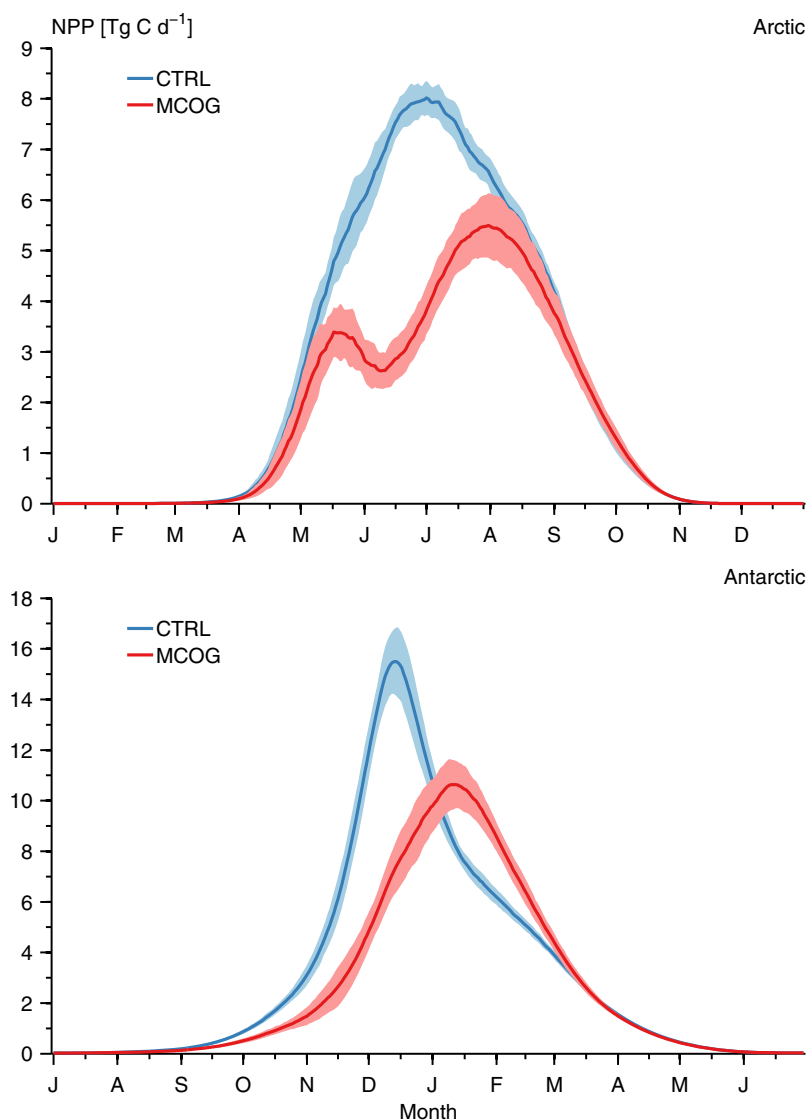


**Figure 6.** Annual net primary production in the (a) Arctic (>65.5°N) and (b) Antarctic region (>60°S) from CTRL (blue) and MCOG (red). Shading shows the standard deviation of interannual variability over 30 years of simulation.

The impact of the MCOG treatment on the Antarctic bloom is similar to those in the Arctic, though the regional variation producing a dual peak is not present. Antarctic NPP in November and December is strongly reduced by the MCOG treatment, a delay that is clearly attributable to the stronger imprint of sea ice distributions on NPP (Figure 7). By early summer (January–February), Antarctic NPP in MCOG actually exceeds that in CTRL (Figure 6), an affect that is again attributable to postponing nutrient consumption resulting in alleviation of late season limitation (Figure 7).

**Table 1.** Annual Net Primary Productivity (NPP; Tg yr<sup>-1</sup>; mean ± 1σ) in Each Region in the Control (CTRL) and Multicolumn Ocean Grid (MCOG) Experiments<sup>a</sup>

	Total		Ice Thickness Category					
	CTRL	MCOG	Open Water	0.1–0.64 m	0.64–1.4 m	1.4–2.5 m	2.5–4.6 m	4.6–9.3 m
Arctic	876 ± 26.6	597 ± 47.1	524 ± 40.7	31.0 ± 4.8	28.0 ± 4.8	12.5 ± 2.6	1.9 ± 0.5	0.0
Antarctic	1202 ± 27.2	970 ± 42.9	920 ± 44.3	40.4 ± 3.5	9.8 ± 1.9	0.6 ± 0.2	0.0	0.0

<sup>a</sup>NPP by each open water and ice thickness category is also shown for MCOG.

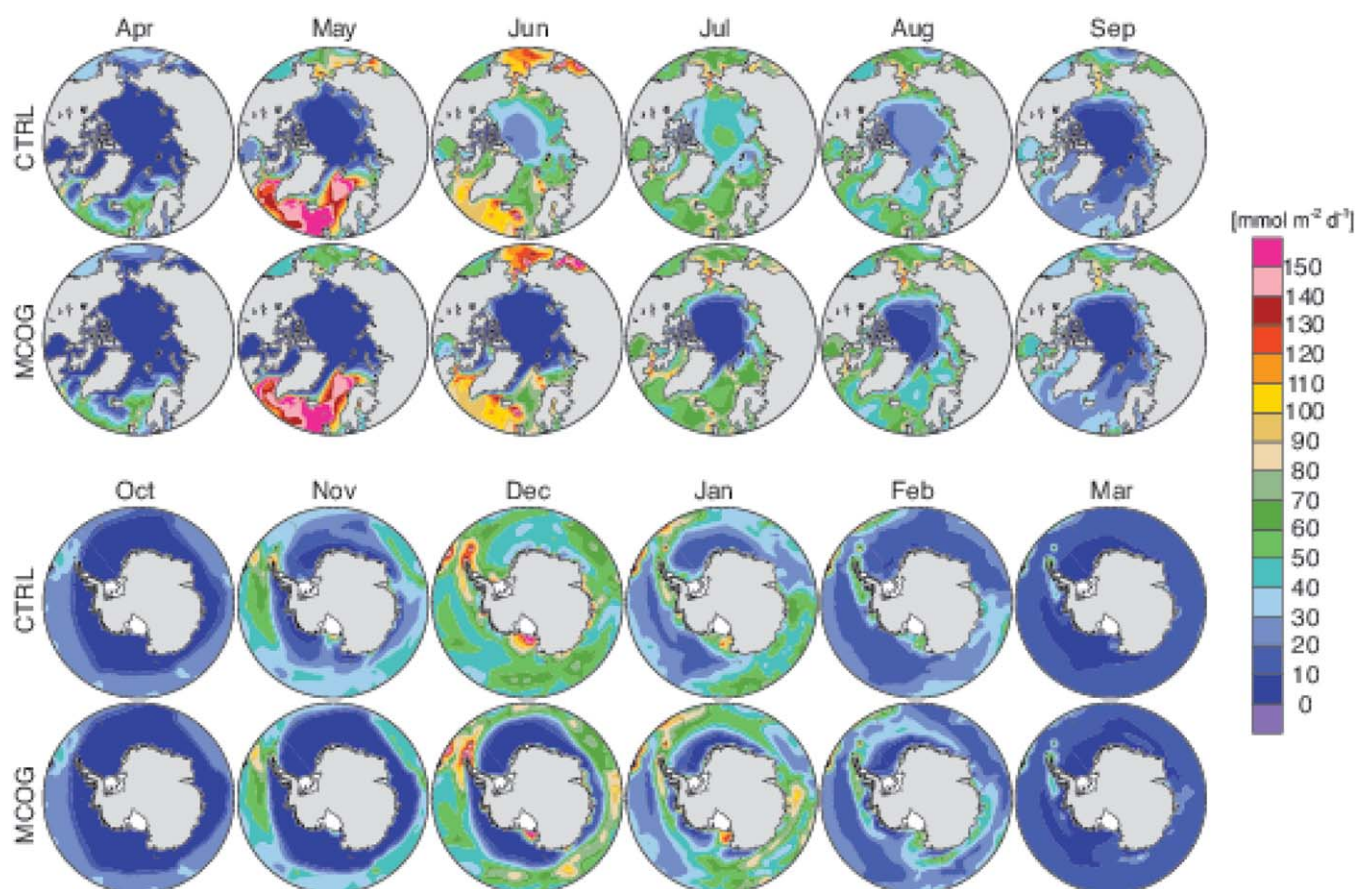


**Figure 7.** Monthly climatologies of spring and summer net primary productivity in the Arctic and Antarctic in the CTRL and MCOG integrations. Units are in terms of  $\text{mmol C m}^{-2} \text{d}^{-1}$ .

We can compute NPP under each ice category from the MCOG experiment, noting that while the light limitation terms have subgrid-scale variation, algal biomass and nutrient limitation remain as aggregate, grid-cell mean quantities. The vast majority of annual production is accomplished in open water regions in both hemispheres. Indeed, open water regions account for about 88% of annual production in the Arctic and roughly 95% of production in the Antarctic (Table 1). While NPP in open water areas dominates annual production, under-ice NPP in midsummer is comparable to that in open water; in the Arctic, for instance, NPP under the two thinnest ice categories is 20–80% of the open water rates (Figure 8). In spite of these relatively high summertime rates, the contribution of the thinner ice thickness categories to the annual regional production is limited by their areal extent. Indeed, at the time of peak production in August, the thinner ice categories account for less than 25% of the total Arctic area (Figure 3a). Below-ice production in the Antarctic is a less significant fraction of the regional total than in the Arctic due to lower below-ice PAR and greater reductions in ice cover during the growing season (Figure 3).

#### 4.4. Surface Chlorophyll Comparison

The changes in NPP produced by MCOG are associated with dramatic reductions in chlorophyll. Figure 9 shows monthly mean surface chlorophyll in SeaWiFS observations [NASA Ocean Biology, 2014], CTRL, and MCOG; Figure 10 shows regional means of these data. While the model integrations are preindustrial simulations, twentieth century climate change does not cause dramatic changes in the chlorophyll distributions in CESM, so a comparison to modern observations is appropriate. A minor caveat in this context, discussed above, is that the simulated sea ice is thicker and more extensive than in twentieth century simulations, but this does not impact the MCOG/CTRL comparison, since these simulations have identical sea ice distributions.

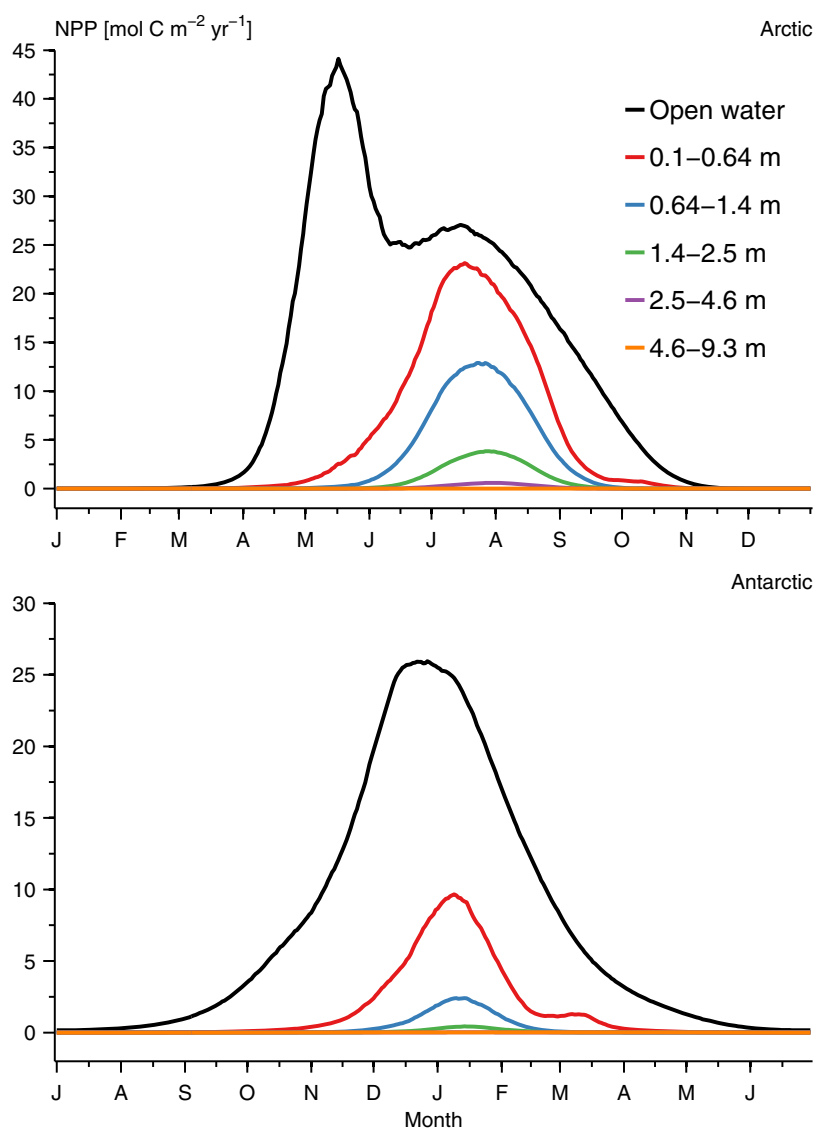


**Figure 8.** Net primary productivity in the (top) Arctic ( $>65.5^\circ\text{N}$ ) and (bottom) Antarctic region ( $>60^\circ\text{S}$ ) separated by ice thickness category in the MCOG simulation.

In a spatial sense, the impact of MCOG on surface chlorophyll is most pronounced in the central Arctic north of Greenland and the Canadian Archipelago where there is persistent ice cover. In this region, the summer-time mean chlorophyll is reduced by 2 orders of magnitude, from values approaching  $10 \text{ mg m}^{-3}$  in CTRL to a seasonal mean less than  $0.1 \text{ mg m}^{-3}$ . Unfortunately, this region is virtually entirely missing from the satellite observations (Figure 9). The impact of MCOG on surface chlorophyll is most significant in spring in both hemispheres (Figures 9 and 10) when light limitation is a dominant control on the bloom and sea ice strongly mediates light distributions. Indeed, these strong reductions in springtime surface chlorophyll amount to a substantial reduction in regional biases relative to the available SeaWiFS observations (Figure 10). The MCOG simulation has higher regional average chlorophyll than CTRL later in the growing season (Figure 10), which is consistent with regionally higher NPP in MCOG relative to CTRL in late summer caused by delayed nutrient consumption postponing seasonal nutrient limitation. Overall, there are several features of the SeaWiFS chlorophyll distribution that are not well simulated by either CTRL or MCOG, pointing to the fact that the model biases are attributable to processes other than light limitation dynamics. However, the dramatic reductions in springtime surface chlorophyll are clearly an improvement in the solution, and an indication of the benefits of considering the impacts of sea ice-induced heterogeneity in the light field.



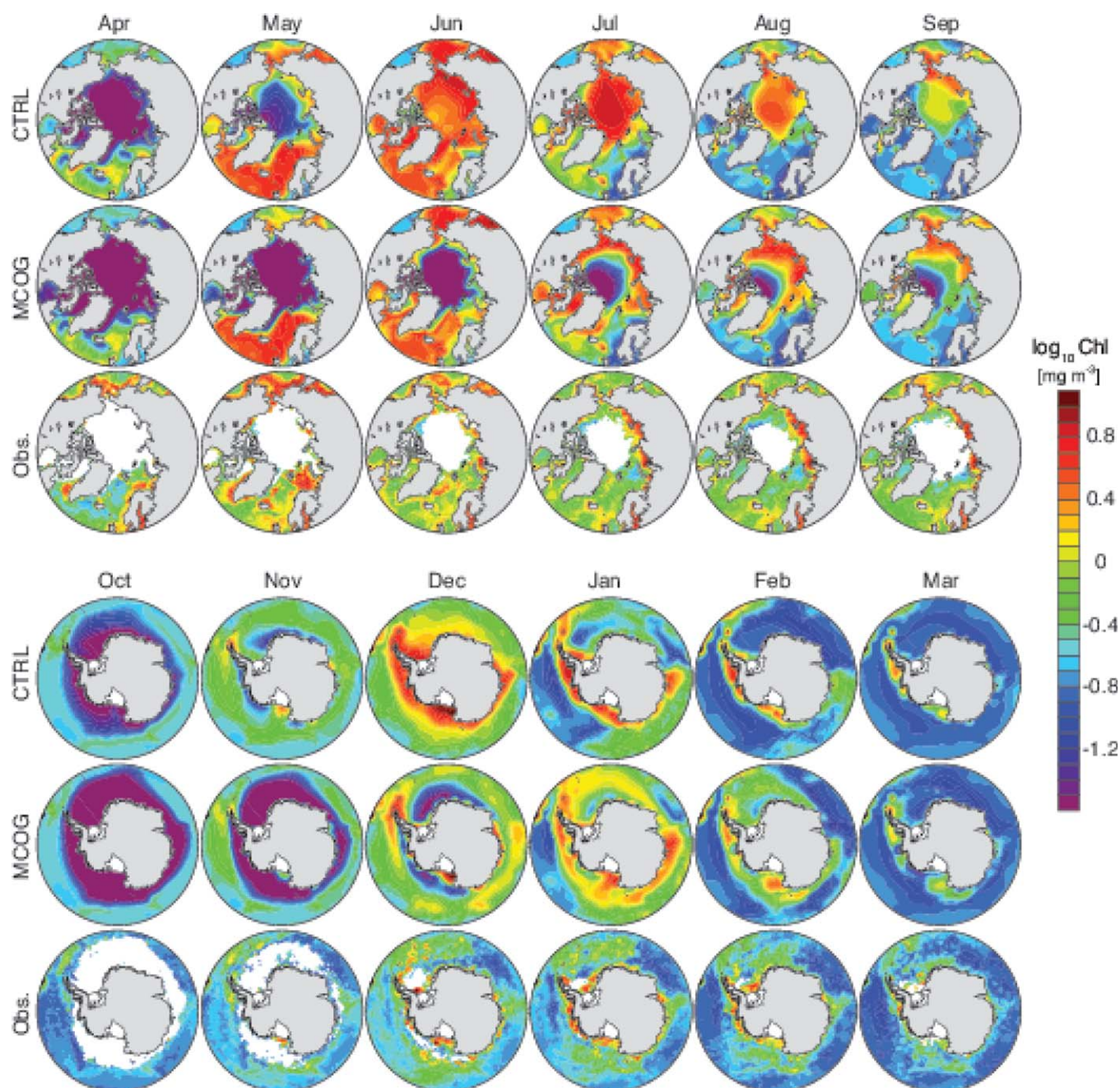


**Figure 9.** Monthly climatologies of spring and summer surface chlorophyll (log transformed) in the Arctic and Antarctic in the CTRL and MCOG integrations as well as SeaWiFS observations (1997–2010).

#### 4.5. Interannual Variability

In addition to changing the mean seasonal patterns of NPP and chlorophyll, the MCOG simulation shows greater interannual variability in production. For instance, while the mean annual production is reduced in both regions, the standard deviation of annual production increases by 55–75% (Table 1). Variability in annual production increases because NPP becomes more sensitive to sea ice distributions; variability in sea ice cover, therefore, more strongly imprints variability in NPP. As discussed in section 2.2, the MCOG treatment inherently yields a stronger dependence on variations in ice fraction for incident irradiance values above about  $30 \text{ W m}^{-2}$  and ice fractions below about 0.8 (Figure 2). Indeed, the majority of NPP in both hemispheres in the model is accomplished in this region of ice-fraction-irradiance phase space (Figure 11),

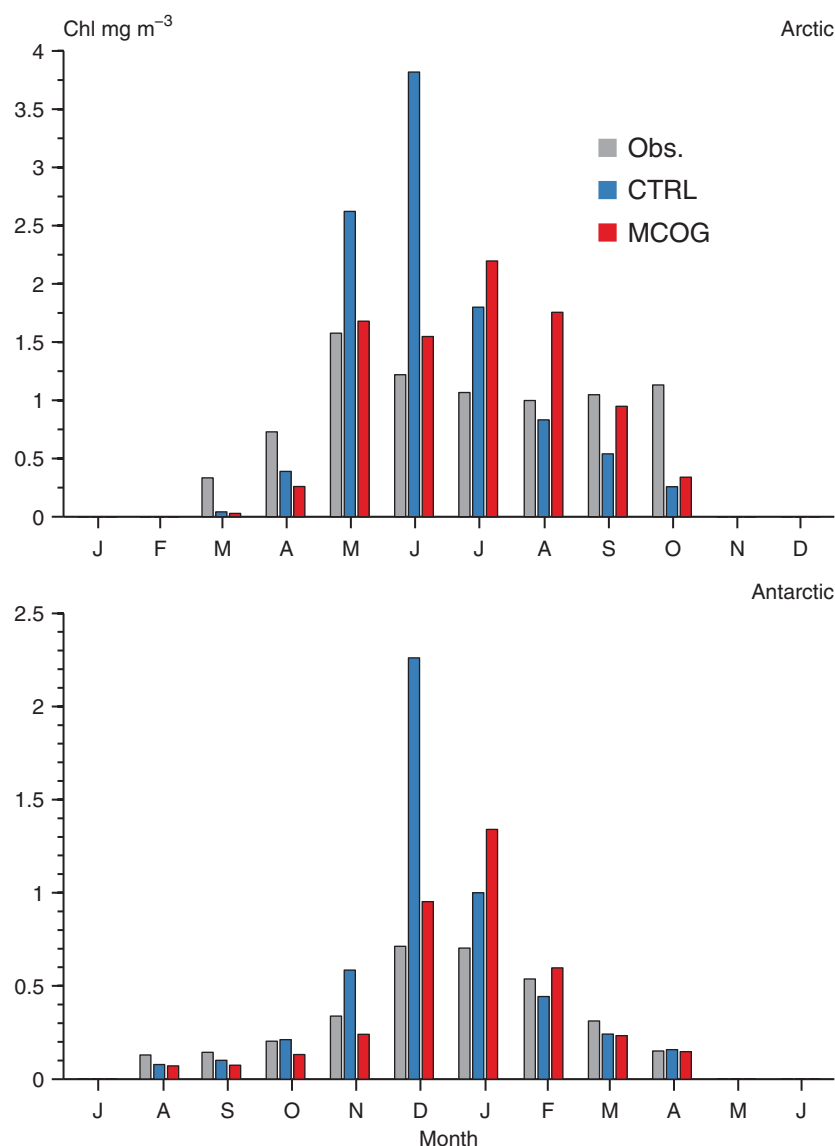


**Figure 10.** Monthly means of surface chlorophyll in the Arctic and Antarctic in the CTRL and MCOG integrations as well as SeaWiFS observations (1997–2010). Areas where SeaWiFS data are missing are not included in the model averages.

consistent with an increase in NPP variability. Notably, the MCOG simulation shows a dramatic increase in the strength of the annual production versus open water relationship (Figure 12, Table 2). Figure 12 shows the relationship between open water area and annual production anomalies for CTRL and MCOG. Recall that these simulations have identical open water distributions and in MCOG the mean annual production is reduced. A greater sensitivity to sea ice distributions means that increased open water area yields proportionally larger positive annual production anomalies in MCOG than in CTRL; conversely, decreased open water area is associated with greater reductions in production in MCOG than CTRL. Therefore, the increased variability in MCOG manifests as an expansion on both sides of the annual mean production probability distribution. Arctic annual production is more sensitive to annual open water area than in the Antarctic. However, while the slope of this relationship more than doubles for the Arctic in MCOG, it increases by about fivefold in the Antarctic, though the variance explained remains relatively low compared to the same relationship in the Arctic (Table 2). The majority of NPP in the Antarctic occurs at lower ice fractions than in the Arctic (Figure 11) thereby sampling a region of ice-fraction-irradiance phase space where the MCOG treatment introduced steep gradients with respect to ice cover in the light limitation function (Figure 2).

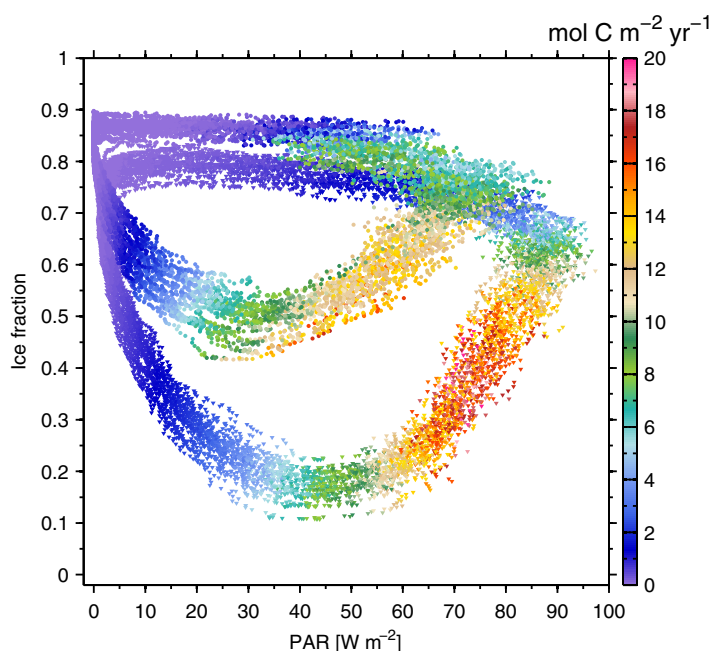


**Figure 11.** Regional-mean ice fraction and surface irradiance (PAR) phase diagram showing daily mean net primary productivity in color from the 30 year MCOG simulation. Circles show data from the Arctic; triangles show data from the Antarctic.

## 5. Discussion

Our results demonstrate the importance of considering subgrid-scale heterogeneity of physical variables when integrating the functions representing nonlinear metabolic rate processes. Computing photosynthesis using mean light fields in the presence of heterogeneity will yield systematic positive biases in NPP. We have demonstrated that accounting for subgrid-scale light heterogeneity in the photosynthesis calculation in ice-covered waters has a dramatic impact on simulated NPP fields in polar regions. In particular, we show strong reductions in NPP accompanied by shifts in the annual bloom timing.

Our results also document that in CESM most of the light supporting NPP in sea ice zones enters the ocean through open water. In the Arctic, CESM predicts that about 12% of annual production is supported by light penetrating through sea ice. Observations document subice phytoplankton blooms, likely fueled by light penetration through sea ice [e.g., Arrigo *et al.*, 2012; Mundy *et al.*, 2014]; however, quantitative estimates of the regional significance of these blooms is lacking.

In addition to reducing the mean NPP in waters partially covered by sea ice, the MCOG treatment tightens the coupling between NPP distributions and sea ice variability. This tighter coupling manifests as a delay in bloom onset, due to stronger dependence on the timing and spatial pattern of ice retreat. Furthermore, the MCOG treatment causes significant increases in interannual variability of production. Given this relationship, we might also expect that secular trends, such as declines in sea ice coverage from climate warming, will drive a proportionally larger NPP response in MCOG versus CTRL. While this behavior will have a modest impact on the model-projected carbon cycle and ecosystem dynamics, the changes in the mean state produced with MCOG are likely more significant than the enhanced sensitivity to sea ice trends.

The MCOG treatment appears to reduce the large, positive springtime surface chlorophyll biases evident in CTRL. In the context of this paper, however, the comparison of modeled fields with observations is complicated by a variety of factors. First, we would ideally validate the model against observed NPP not chlorophyll, since NPP is more relevant to the carbon cycle simulation and not complicated by the photoadaptation response. However, observations of NPP at the scales of interest are not available and local comparisons of the coarse resolution model to in situ observations are complicated by representation errors [e.g., Oke and Sakov, 2008] among other issues, including a paucity of measurements under sea ice. A comparison with SeaWiFS chlorophyll is limited by a sampling bias inherent in the satellite observations, which do not integrate chlorophyll beneath sea ice and are therefore biased to times of open water. Furthermore,



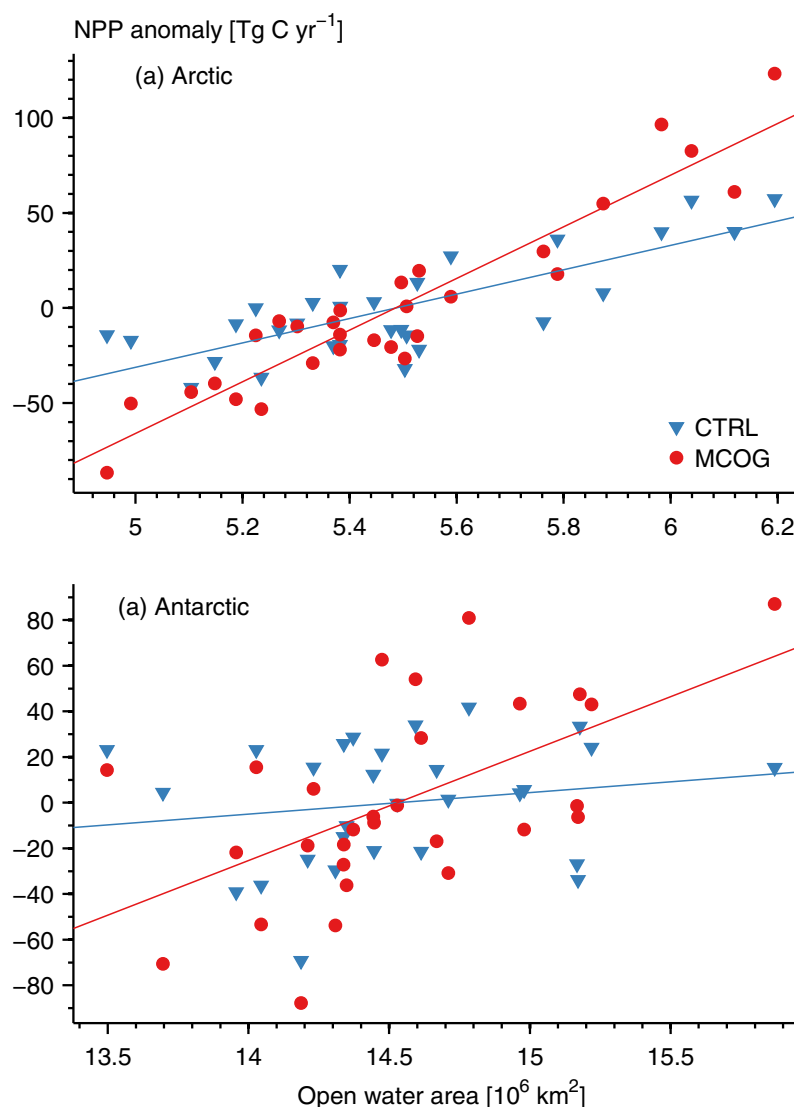


**Figure 12.** Annually integrated net primary productivity (NPP) anomaly relative to long-term mean versus mean summertime open water area in the (a) Arctic (JAS) and (b) Antarctic (JFM) regions. Note that CTRL and MCOG have different mean NPP, thus we are plotting anomalies, whereas their ice distributions are identical.

large regions of the central Arctic—the region with the strongest MCOG effect—are entirely missing from the satellite observations. In addition to these methodological limitations, there is a conceptual problem with the observational comparison in the context of evaluating the MCOG implementation: large-scale biases in CTRL are not simply a manifestation of inappropriate treatment of subgrid-scale heterogeneity in light, rather they result from a superposition of model deficiencies. There is no reason to strongly expect that fixing a particular process representation will improve the overall solution; indeed, it may in fact degrade the model solution as bias cancelation is relaxed. On this basis, we would argue for the implementation of MCOG even if it degraded solutions because it is simply a more accurate invocation of the model equations. In spite of these caveats, dramatic reductions in springtime chlorophyll in MCOG appear to be a genuine improvement in the model; later season dynamics are less tightly controlled by the light limitation effect, so an increase in model bias during this period may reflect biased nutrient distributions and other deficiencies.

Ultimately, the changes in NPP in the new MCOG photosynthesis treatment result from the concave-downward shape of the PI-curve. The PI-curve increases approximately linearly at low irradiance, and is fairly flat at high irradiance (Figure 1). Given this characteristic shape, error associated with neglecting subgrid-

**Table 2.** Linear Regression Results of Annual Net Primary Production Versus Summertime-Mean Open Water Area ( $\text{Tg yr}^{-1} (10^6 \text{ km}^2)^{-1}$ )

	Arctic		Antarctic	
	CTRL	MCOG	CTRL	MCOG
Slope	$64.1 \pm 20.1$	$136 \pm 19.9$	$9.4 \pm 21.0^{\text{ns}}$	$47.8 \pm 27.8$
$r^2$	0.6121	0.8785	0.0303	0.3154
$p$	<0.001	<0.001	0.367	0.002

scale irradiance variability is a function of both the mean irradiance and the variability about that mean. At high grid-cell mean irradiance, the photosynthesis computation samples a portion of the PI-curve that is relatively flat and thus the MCOG correction is small. Conversely, when irradiance is low or spanning a large

range, the MCOG correction tends to be fairly large. Figure 13 summarizes this, showing the mean difference between the MCOG and CTRL light limitation terms for the model diatom functional type as a function of subgrid-scale variability in irradiance and grid-cell mean irradiance. The largest effect occurs where grid-cell mean irradiance is below about  $30 \text{ W m}^{-2}$  and the standard deviation of subgrid-scale irradiance is between about 20 and  $40 \text{ W m}^{-2}$ . This pattern is consistent with the largest MCOG effect in Spring, when light levels remain low enough to sample strong curvature in the P-I relationship. The photosynthetic parameters used to define the PI-curve (see section 2.2) impact its shape and will thus change the structure of the MCOG correction. For instance, smaller values of  $\alpha^{\text{chl}}$  reduce the concavity of the PI-curve, thereby diminishing the magnitude of the MCOG correction and the region over phase space where it is most significant.

The structure of the MCOG correction is a property of the PI-curve and is thus applicable more generally to any situation where photosynthesis is computed from mean light fields that aggregate substantial variability. Sea ice is an obvious mechanism producing variation in irradiance in space; a comparable phenomenon may occur in time, due to fluctuations in irradiance below the time step level. The CESM ocean component includes a diurnal cycle for light and is typically integrated with a 1 h time step. To the extent that light varies substantially on intervals below an hour, the model will generate positive biases in NPP with a pattern similar to that in Figure 13.

While the MCOG treatment of photosynthesis is a more accurate invocation of the model equations for photosynthesis than using grid-cell mean light at coarse resolution, it is not a complete subgrid-scale model, as ocean tracers remain homogenous within a grid-cell. This precludes representation of the time-accruing

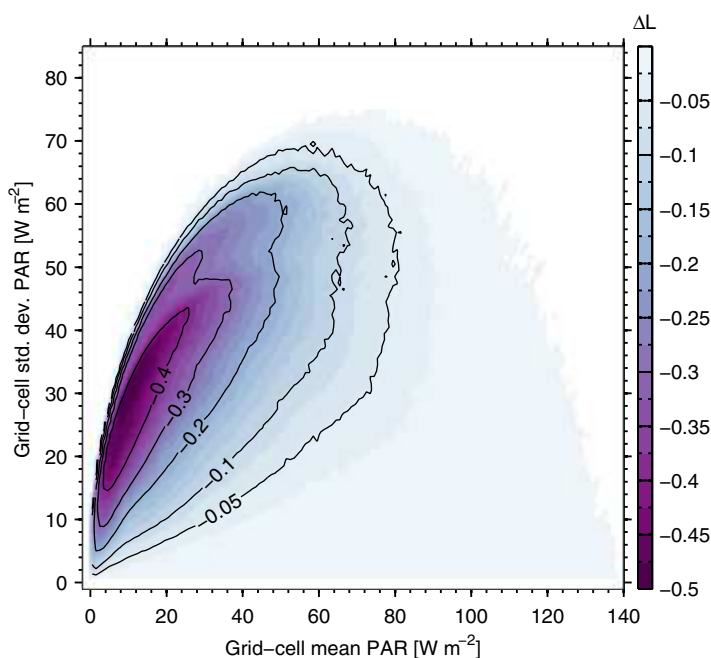


**Figure 13.** Mean difference between MCOG and CTRL light limitation terms as a function of area-weighted, grid-cell standard deviation and mean photosynthetically available radiation (PAR).

impacts of persistent open water conditions at subgrid-scales on biomass accumulation and subsequent localized nutrient limitation, for instance. Treatment of such subgrid-scale features is a challenge in the traditional ocean modeling framework, since advection and mixing tendencies are computed on the actual model grid and do not account for subgrid-scale variation in tracers. As a general topic, the question of how subgrid-scale variation in physical forcing manifests as nonlinear perturbations in biological fields merits further research and extends beyond the realm of sea ice-induced heterogeneity. Indeed, the mean field approximation generates errors when applied in the context of submesoscale and mesoscale ocean turbulence [e.g., *Levy and Martin*, 2013]. Another sea ice-related process worth noting is the treatment of aeolian iron deposition in CESM. In the integrations presented here, atmospheric iron deposition does not interact with sea ice but is simply passed through to the surface ocean. Recent development efforts have added the capability for sea ice to intercept and accumulate iron, leading to changes in the seasonal timing of iron release and transport, with implications for both Arctic and Antarctic NPP [*Wang et al.*, 2014].

The MCOG treatment introduces a small additional computational burden in the model. In the runs we present, the ocean component in the MCOG simulation is about 5% more costly than in CTRL, though more careful treatment of the code could potentially reduce this increment. The cost of the MCOG implementation could be further reduced by operating on binned ice thickness categories, thereby reducing the number of light limitation function evaluations. Figures 5 and 6 suggest that the two thickest ice categories could be aggregated into one, since they are similar and support minuscule NPP. A fixed binning strategy would require some a priori knowledge of the light transmittance properties across categories; alternatively, it is conceivable that binning could be done dynamically at the time step level. A binning strategy, and the basic ice thickness categories themselves, can impact the MCOG solution since aggregation limits the resolution of subgrid-scale variability in PAR. Indeed, the extent to which light transmittance varies within categories will produce an effect similar to that observed at the grid-scale. On this basis, improved resolution in the ice thickness categories that transmit significant light would improve the accuracy of the MCOG treatment, though the marginal benefit of such an approach would depend on the within-category variation in light transmittance. Indeed, the MCOG treatment would be applicable to sea ice models with only one ice category; since the distinction between open water and ice is pronounced, these models would also likely benefit from the model developments discussed here (although not to the full extent of a multicategory model).

In summary, the MCOG solution is an improvement to the default version of the CESM marine biogeochemistry model; it provides a more physically justified treatment of photosynthesis that is more consistent across sea ice-covered and open water regions. Simulations with the MCOG implementation lead to reduced NPP and chlorophyll in polar waters, particularly in springtime, yielding a solution that is more consistent with available satellite observations. Finally, in addition to strongly impacting the mean state, MCOG enhances the sensitivity of photosynthesis to sea ice conditions, thereby augmenting the variability in simulated NPP.

# Acknowledgments

The authors thank Bruce Briegleb and Nancy Norton for their work on implementing the multicolumn capabilities in CESM. Thanks is also given to Gokhan Danabasoglu for useful discussions and to the anonymous reviewers for their insightful comments and suggestions. M.C.L. acknowledges NSF support (OCE-1048926) and M.M.H. also acknowledges NSF support (PLR-0968703). Computational facilities have been provided by the Climate Simulation Laboratory, which is managed by CISL at NCAR. NCAR is supported by the National Science Foundation. The CESM source code is freely available at <http://www2.cesm.ucar.edu>. The model output described in this paper can be obtained by contacting the lead author ([mclong@ucar.edu](mailto:mclong@ucar.edu)).

# References

- Arrigo, K. R., et al. (2012), Massive phytoplankton blooms under Arctic Sea ice, *Science*, 336, 1408, doi:10.1126/science.1215065.
- Briegleb, B., and B. Light (2007), A delta-Eddington multiple scattering parameterization for solar radiation in the sea ice component of the community climate system model, *NCAR Tech. Note NCAR/TN-472+STR*, Nat. Cent. Atmos. Res., Boulder, Colo., doi:10.5065/D6B27S71.
- Comiso, J. C. (2000), *Bootstrap Sea Ice Concentrations From Nimbus-7 SMMR and DMSP SSM/I-SSMIS*, NASA Natl. Snow and Ice Data Cent. Distrib. Active Arch. Cent., Boulder, Colo., doi:10.5067/J6JQLS9EJ5HU.
- Danabasoglu, G., S. C. Bates, B. P. Briegleb, S. R. Jayne, M. Jochum, W. G. Large, S. Peacock, and S. G. Yeager (2012), The CCSM4 ocean component, *J. Clim.*, 25(5), 1361–1389, doi:10.1175/JCLI-D-11-00091.1.
- Dunne, J., A. Gnanadesikan, J. L. Sarmiento, and R. D. Slater (2010), Technical description of the prototype version (v0) of tracers of phytoplankton with allometric zooplankton (TOPAZ) ocean biogeochemical model as used in the Princeton IFMIP model, *Biogeosciences*, 7, supplement, 3593–3624, doi:10.5194/bg-7-3593-2010.
- Dutkiewicz, S., M. J. Follows, and P. Parekh (2005), Interactions of the iron and phosphorus cycles: A three-dimensional model study, *Global Biogeochem. Cycles*, 19, GB1021, doi:10.1029/2004GB002342.
- Falkowski, P., and J. Raven (2007), *Aquatic Photosynthesis*, Blackwell Sci., Princeton University Press, Princeton, N. J.
- Falkowski, P., et al. (2000), The global carbon cycle: A test of our knowledge of earth as a system, *Science*, 290, 291–296, doi:10.1126/science.290.5490.291.
- Fetterer, F., K. Knowles, W. Meier, and M. Savoie (2002), *Updated Daily Sea Ice Index [1979–2012]*, Natl. Snow and Ice Data Cent., Boulder, Colo., doi:10.7265/N5QJ7F7W.
- Geider, R., H. MacIntyre, and T. Kana (1998), A dynamic regulatory model of phytoplankton acclimation to light, nutrients, and temperature, *Limnol. Oceanogr.*, 43, 679–694.
- Gent, P. R., et al. (2011), The community climate system model version 4, *J. Clim.*, 24(19), 4973–4991, doi:10.1175/2011JCLI4083.1.
- Holland, M. M. (2003), An improved single-column model representation of ocean mixing associated with summertime leads: Results from a SHEBA case study, *J. Geophys. Res.*, 108, 3107, doi:10.1029/2002JC001557.

- Holland, M. M., and L. Landrum (2015), Factors affecting projected arctic surface shortwave heating and albedo change in coupled climate models, *Philos. Trans. R. Soc. A*, 373, 20140162, doi:10.1098/rsta.2014.0162.
- Holland, M. M., C. M. Bitz, E. C. Hunke, W. H. Lipscomb, and J. L. Schramm (2006), Influence of the sea ice thickness distribution on polar climate in CCSM3, *J. Clim.*, 19, 2398–2414, doi:10.1175/JCLI3751.1.
- Holland, M. M., D. A. Bailey, B. P. Briegleb, B. Light, and E. Hunke (2012), Improved sea ice shortwave radiation physics in CCSM4: The impact of melt ponds and aerosols on Arctic Sea ice, *J. Clim.*, 25(5), 1413–1430, doi:10.1175/JCLI-D-11-00078.1.
- Hunke, E., and W. Lipscomb (2008), CICE: The Los Alamos Sea Ice Model, documentation and software user's manual, version 4.0, *Tech. Rep. LA-CC-06-012*, Los Alamos Natl. Lab, Los Alamos, N. M.
- Hurrell, J. W., et al. (2013), The Community Earth System Model: A framework for collaborative research, *Bull. Am. Meteorol. Soc.*, 94, 1339–1360, doi:10.1175/BAMS-D-12-00121.1.
- Jahn, A., et al. (2012), Late-twentieth-century simulation of arctic sea ice and ocean properties in the ccsm4, *J. Clim.*, 25(5), 1431–1452, doi:10.1175/JCLI-D-11-00201.1.
- Kay, J. E., et al. (2014), The Community Earth System Model (CESM) Large Ensemble project: A community resource for studying climate change in the presence of internal climate variability, *Bull. Am. Meteorol. Soc.*, doi:10.1175/BAMS-D-13-00255.1.
- Kwok, R., G. F. Cunningham, M. Wensnahan, I. Rigor, H. J. Zwally, and D. Yi (2009), Thinning and volume loss of the Arctic Ocean sea ice cover: 2003–2008, *J. Geophys. Res.*, 114, C07005, doi:10.1029/2009JC005312.
- Landrum, L., M. M. Holland, D. P. Schneider, and E. Hunke (2012), Antarctic Sea ice climatology, variability, and late twentieth-century change in CCSM4, *J. Clim.*, 25(14), 4817–4838, doi:10.1175/JCLI-D-11-00289.1.
- Lengaigne, M., G. Madec, L. Bopp, C. Menkes, O. Aumont, and P. Cadule (2009), Bio-physical feedbacks in the Arctic Ocean using an Earth system model, *Geophys. Res. Lett.*, 36, L21602, doi:10.1029/2009GL040145.
- Levy, M., and A. P. Martin (2013), The influence of mesoscale and submesoscale heterogeneity on ocean biogeochemical reactions, *Global Biogeochem. Cycles*, 27, 1139–1150, doi:10.1002/2012GB004518.
- Long, M. C., K. Lindsay, S. Peacock, J. K. Moore, and S. C. Doney (2013), Twentieth-century oceanic carbon uptake and storage in CESM1(BGC), *J. Clim.*, 26(18), 6775–6800, doi:10.1175/JCLI-D-12-00184.1.
- McPhee, M. (2008), *Air-Ice-Ocean Interaction: Turbulent Ocean Boundary Layer Exchange Processes*, Springer, N. Y., doi:10.1007/978-0-387-78335-2.
- Meehl, G. A., et al. (2013), Climate change projections in cesm1(cam5) compared to ccsm4, *J. Clim.*, 26(17), 6287–6308, doi:10.1175/JCLI-D-12-00572.1.
- Moore, J. K., S. C. Doney, J. A. Kleypas, D. M. Glover, and I. Y. Fung (2002), An intermediate complexity marine ecosystem model for the global domain, *Deep Sea Res., Part II*, 49(1–3), 403–462, doi:10.1016/S0967-0645(01)00108-4.
- Moore, J. K., K. Lindsay, S. C. Doney, M. C. Long, and K. Misumi (2013), Marine ecosystem dynamics and biogeochemical cycling in the Community Earth System Model [CESM1(BGC)]: Comparison of the 1990s with the 2090s under the RCP4.5 and RCP8.5 scenarios, *J. Clim.*, 26(23), 9291–9312, doi:10.1175/JCLI-D-12-00566.1.
- Mundy, C., et al. (2014), Role of environmental factors on phytoplankton bloom initiation under landfast sea ice in Resolute Passage, Canada, *Mar. Ecol. Prog. Ser.*, 497, 39–49, doi:10.3354/meps10587.
- NASA Ocean Biology (2014), Sea-viewing Wide Field-of-view Sensor (SeaWiFS) Ocean Color Data, 2014.0 Reprocessing, NASA OB.DAAC, Greenbelt, Md., doi:10.5067/ORBVIEW-2/SEAWIFS\_OC.2014.0.
- Oke, P. R., and P. Sakov (2008), Representation error of oceanic observations for data assimilation, *J. Atmos. Oceanic Technol.*, 25, 1004–1017, doi:10.1175/2007JTECHO558.1.
- Smith, R. D., et al. (2010), The Parallel Ocean Program (POP) reference manual, *Tech. Rep. LAUR-10-01853*, Los Alamos Natl. Lab, Los Alamos, N. M. [Available at <http://www.cesm.ucar.edu/models/cesm1.0/pop2/doc/sci/POPRefManual.pdf>.]
- Thorndike, A. S., D. A. Rothrock, G. A. Maykut, and R. Colony (1975), The thickness distribution of sea ice, *J. Geophys. Res.*, 80, 4501–4513, doi:10.1029/JC080i033p04501.
- Wang, S., D. Bailey, K. Lindsay, J. K. Moore, and M. Holland (2014), Impact of sea ice on the marine iron cycle and phytoplankton productivity, *Biogeosciences*, 11, 4713–4731, doi:10.5194/bg-11-4713-2014.
- Worby, A. P., C. A. Geiger, M. J. Paget, M. L. van Woert, S. F. Ackley, and T. L. Deliberty (2008), Thickness distribution of Antarctic sea ice, *J. Geophys. Res.*, 113, C05S92, doi:10.1029/2007JC004254.